-RESEARCH PAPER-

International Journal of Mining and Geo-Engineering

IJMGE

IJMGE 58-1 (2024) 97-104

DOI: 10.22059/ijmge.2023.369656.595130

Numerical simulation of matrix acidizing in carbonate formations using method of lines

Saman Jahanbakhshi [a]

[a] *School of Mining Engineering, College of Engineering, University of Tehran, Tehran, Iran.*

Article History:

Received: 15 December 2023.

Revised: 23 December 2023.

Accepted: 31 December 2023.

ABSTRACT

In this study, a novel numerical approach is proposed to characterize the dissolution of rock minerals and wormhole propagation in carbonate rocks using the Darcy scale model. Accordingly, only the spatial variables of the governing partial differential equations are discretized, while the time variable remains continuous. Consequently, the partial differential equations are turned into ordinary ones, which are then numerically solved by high-order Runge-Kutta methods. The proposed approach is verified against the analytical solution in a 1D core model. Afterwards, it will be utilized to investigate the effect of multiple transport and reaction phenomena on the matrix acidizing in 2D carbonate formations. Also, the staggered grid technique is employed to accurately predict the wormhole patterns during several injection regimes. Compared to the previous studies, the proposed numerical approach is less complicated and straightforward. Furthermore, the computational cost is more affordable.

Keywords: *Carbonate reservoirs, Matrix acidizing, Rock dissolution, Darcy scale model, Numerical simulation.*

1. Introduction

During the production time of an oil or gas well, the migration of fine particle from the reservoir rock causes the permeability of the near wellbore area to decrease significantly [1]. Accordingly, a thin damaged region with low permeability is created around the wellbore, which poses additional pressure drop. This kind of formation damage is the called skin factor in petroleum literature [2]. Multiple well stimulation techniques, such as matrix acidizing, have been proposed to remove this damage and increase the productivity of well.

According to the census statistics, most of the available petroleum reserves exist in the carbonate reservoirs [3]. In these reservoirs, acid is injected without fracturing the reservoir rock and dissolves the rock minerals, creating high conductive wormholes. These wormholes provide least resistant pathways through which oil and the gas reach the wellbore, thus the well productivity is improved [4]. Obviously, a successful well stimulation technique depends on the costs of the operations compared to the incremental productivity index.

In carbonate reservoirs, formation is mainly composed of calcite and dolomite minerals; thus, hydrochloric acid is an appropriate choice. The evolution of wormholes and promotion of permeability depend on different factors, such as the rate of the acid injection, reaction kinetics, temperature, and structural properties of porous media [5, 6].

Substantial studies have been performed to investigate the inherent complexity of the dissolution process in matrix acidizing [7-10]. Also, theoretical studies for modeling the dissolution phenomena are classified into four categories [11]: dimensionless model [12], capillary tube approach [13], pore scale model [14, 15], and continuum-based model [11, 16, 17]. In the dimensionless model, the dissolution of carbonate rocks is assumed to be similar to the reaction of acid in a single capillary tube. Consequently, the controlling dimensionless groups are identified and the optimum rate of acid injection is determined [18]. However, the number of required parameters is large and this approach cannot estimate the appropriate pore volumes of acid for breakthrough. In the capillary tube approach, a pre-defined cylindrical shape of the wormhole is considered and the transport of reaction of the acid is studied therein. Accordingly, this approach is unable to predict different dissolution patterns which makes it impractical for the prediction of core scale experiments. In the pore scale model, a bundle of inter-connected capillary tubes is used to represent the reservoir rock. The acid reacts with the walls of the tubes; thus, increases their radii. Pore scale model provides a qualitative prediction of the dissolution patterns. Also, the predicted pore volumes highly overestimate the experimental results. Later Hoefner and Fogler [19] extended the pore scale model and proposed physically representative network model. Again, the predicted pore volumes were unreasonably high compared to the experimental investigations. In comparison, continuum-based models more precisely describe the propagation of wormholes throughout the carbonate rocks.

In the continuum-based model, which is also the approach of the current study, the momentum equation (Darcy's law), transport of diluted species, and rock/fluid reaction are coupled. Furthermore, acid dissolution changes the rock structure at different length scales. From Darcy's scale point of view, porosity and permeability of the rock changes. However, pore radius, pore connectivity and interfacial area alter at the pore scale. Consequently, an appropriate correlation is required to relate these properties at different length scales.

Because of the inherent coupling between the acid transport and its reaction, obtaining a precise solution of the Darcy-scale model is highly challenging and requires an extremely fine mesh structure [17, 20].

* Corresponding author. *E-mail address:* jahanbakhshi@ut.ac.ir (S. Jahanbakhshi).

Accordingly, for a large rock sample or fast reactive fronts, a large number of gridblocks are required which poses a high computational burden. The basic idea here is to solve the system of coupled differential equations by the method of lines (MOL). In the MOL, only the spatial variables of the governing partial differential equations are discretized and the time variable remains continuous. Consequently, the partial differential equations turn into ordinary ones which are then numerically solved by high-order Runge-Kutta methods. Runge–Kutta methods are efficient, long-established and popular techniques for numerical analyzing initial-value problems in differential equations [21]. The Runge–Kutta technique establishes high-order precise solutions by the function itself, and requires none of the function derivatives.

This study is organized as follows: Darcy scale continuum model together with the numerical simulation schemes are described in Section 2. The MOL formulation is also derived here. Section 3 introduces 1D and 2D core models. 1D core model is used to verify the results of the proposed approach. Afterwards, results of the numerical simulation of matrix acidizing in carbonate formations are discussed in Section 4. Then, final conclusions are summarized in Section 5.

2. Methodology

2.1. Darcy scale model

In this study, two-scale continuum model is utilized to illustrate the reactive flow of acid through the carbonate formation. Subsequently, Darcy-scale equations, which are well described by Panga et al. [16], were considered:

$$\mathbf{U} = -\frac{1}{\mu}\mathbf{K}.\nabla P \tag{1}$$

$$\frac{\partial \varphi}{\partial t} + \nabla.\mathbf{U} = 0 \tag{2}$$

Here, $\mathbf{U}, \mu, \mathbf{K}, P$, and φ stand for vector of acid velocity, viscosity of acid, permeability tensor, pressure, and rock porosity, respectively.

According to the experimental investigations, Fredd and Fogler [18] disclosed the fact that the reaction of hydrochloric acid with carbonate rocks follows a linear kinetics. The same assumption is considered by most of previous studies [11, 16, 20, 22]. Furthermore, the change in reaction order only changes the volume of required acid to breakthrough, consequently, the proposed model also remains valid in non-linear kinetics [11]. By assuming linear kinetics, the balance between diffusion, convection, and reaction of injected acid results in,

$$\frac{\partial(\varphi \mathrm{C_f})}{\partial t} + \nabla.(\mathbf{U}\mathrm{C_f}) = \nabla.(\varphi \mathbf{D_e}.\nabla \mathrm{C_f}) - k_c a_v (\mathrm{C_f} - \mathrm{C}_s) \tag{3}$$

$$\mathrm{C}_s = \frac{\mathrm{C_f}}{(1 + k_s / k_c)} \tag{4}$$

Here, $\mathrm{C_f}, \mathrm{C_s}, \mathbf{D_e}, k_s, a_v$, and k_c show the concentration of the injected acid in the liquid phase, the concentration of the acid at the solid face, the tensor of the effective dispersion-diffusion, acid reaction rate, interfacial area between the liquid and the solid, and the local mass transfer coefficient, respectively. The term $k_c a_v(\mathrm{C_f} - \mathrm{C_s})$ stands for the acid transform from the liquid phase to the solid face. Apparently, fluid properties, such as viscosity and density of acid, are assumed to be unaffected by the dissolution process.

Expectedly, matrix acidizing causes the dissolution of the carbonate minerals which is represented by:

$$\frac{\partial \varphi}{\partial t} = \frac{k_c (\mathrm{C_f} - \mathrm{C}_s) a_v \alpha}{\rho_s} \tag{5}$$

Here, α shows the dissolving power of the injected acid and ρ_s is the rock density. Acid dissolution changes the rock structure at different length scales. From Darcy's scale point of view, the porosity and permeability of the rock changes. However, pore radius, pore connectivity, and interfacial area alter at the pore scale. Consequently, an appropriate correlation is required to relate these properties at different length scales. In this study, the Carman–Kozeny correlation is utilized to relate the change in permeability as a result of change in porosity [23],

$$\mathbf{K} = k\,\mathbf{I};\quad \frac{k}{k_0} = \left(\frac{\varphi}{\varphi_0}\right)^{\gamma}\left[\frac{\varphi(1-\varphi_0)}{\varphi_0(1-\varphi)}\right]^{2\beta} \tag{6}$$

where φ_0 and k_0 are the initial porosity and permeability of the rock sample, and φ as well as k are the current porosity and permeability after the acidizing. Also, β is a constant. Furthermore, the variation of pore radius and interfacial area due to the acid reaction is represented by:

$$\frac{a_v}{a_0} = \frac{\varphi\, r_0}{\varphi_0\, r_p} \tag{7}$$

$$\frac{r_p}{r_0} = \sqrt{\frac{k\,\varphi_0}{k_0\,\varphi}} \tag{8}$$

where r_0 and r_p are the initial and current pore radii.

Also, k_c and D_e are calculated from [24]:

$$Sh = \frac{2k_c r_p}{D_m} = Sh_\infty + bRe_p^{1/2} Sc^{1/3} \tag{9}$$

$$Re_p = \frac{2|\mathbf{U}|r_p}{\nu} \tag{10}$$

$$Sc = \frac{\nu}{D_m} \tag{11}$$

$$D_{\mathrm{e,X}} = \alpha_{\mathrm{os}} D_m + \frac{2\lambda_{\mathrm{x}}|\mathbf{U}|r_p}{\varphi},\quad D_{\mathrm{e,T}} = \alpha_{\mathrm{os}} D_m + \frac{2\lambda_{\mathrm{T}}|\mathbf{U}|r_p}{\varphi} \tag{12}$$

Here, $Sh, D_m, Sh_\infty, b, Re_p, Sc$, and ν represent the Sherwood number, coefficient of molecular diffusion, asymptotic Sherwood number, equation constant, Reynolds number, Schmidt number, and acid kinematic viscosity, respectively. Also, $D_{e,X}$ and $D_{e,T}$ show longitudinal and transverse components of the effective dispersion-diffusion tensor, λ_x and λ_T are constants, and α_{os} is a constant for pore connectivity.

Consequently, the boundary and initial conditions required to solve the governing set of differential equations become:

$$u\mathrm{C_f} - \varphi D_{\mathrm{e,X}} \frac{\partial \mathrm{C_f}}{\partial x} = u_0 \mathrm{C}_0,\quad \text{at } x = 0 \tag{13}$$

$$-\frac{k_x}{\mu}\frac{\partial P}{\partial x} = u_0,\quad \frac{\partial P}{\partial y} = 0,\quad \text{at } x = 0 \tag{14}$$

$$n.\nabla P = 0,\quad n.\nabla \mathrm{C_f} = 0,\quad \text{at } y = 0, H \tag{15}$$

$$P = P_e,\quad \frac{\partial \mathrm{C_f}}{\partial x} = 0,\quad \text{at } x = L \tag{16}$$

$$\varphi = \varphi_0 + \hat{f},\quad \mathrm{C_f} = 0,\quad \text{at } t = 0 \text{ and } \hat{f} \in [-\Delta\varphi_0, \Delta\varphi_0] \tag{17}$$

in which u_0, C_0, P_e, L, and $\hat{f}$ show acid velocity at the inlet face, acid concentration at the inlet face, outlet pressure, length of the rock sample, and random fluctuations in the initial porosity, respectively. This fluctuation causes the initiation of wormholes.

Obviously, Danckwert's condition is established at the inlet of the simulation domain, while the Dirichlet boundary condition is established at the outlet. This is due to the fact that at high Da numbers, the injected acid immediately reacts with the calcite minerals, leading to upstream gradients at the inlet face. Accordingly, acid dispersion becomes significant and the traditional Dirichlet boundary condition, proposed by Panga et al. [16], becomes invalid [20]. Also, no-flow condition is considered at the transverse boundaries.

2.2. Dimensionless model equations

The model equations are made dimensionless using dimensionless variables below [11]:

$$\begin{aligned} &x_{\mathrm{D}} = \frac{x}{L},\quad y_{\mathrm{D}} = \frac{y}{L},\quad \mathbf{u}_{\mathrm{D}} = \frac{\mathbf{U}}{u_0},\quad t_{\mathrm{D}} = \frac{t}{(L/u_0)} \\ &r_{\mathrm{D}} = \frac{r_p}{r_0},\quad A_{\mathrm{vD}} = \frac{a_v}{a_0},\quad \kappa_{\mathrm{D}} = \frac{k}{k_0} \\ &\mathrm{c_{fD}} = \frac{\mathrm{C_f}}{\mathrm{C}_0},\quad \mathrm{c_{sD}} = \frac{\mathrm{C_s}}{\mathrm{C}_0},\quad p_{\mathrm{D}} = \frac{P - P_e}{(\mu u_0 L / k_0)} \end{aligned} \tag{18}$$

$$Da=\frac{k_s a_0 L}{u_0},\quad \phi^2=\frac{2k_s r_0}{D_m},\quad \Phi^2=\frac{k_s a_0 L^2}{D_m}$$
$$N_{ac}=\frac{\alpha C_0}{\rho_s},\quad \eta=\frac{2r_0}{L},\quad Pe=\frac{u_0 L}{D_m} \tag{19}$$

Here, Da is the Damköhler number, ϕ^2 is the Thiele modulus at pore scale, Φ^2 is the Thiele modulus at macro scale, N_{ac} shows the acid capacity number, η shows the scale length ratio, and Peshows the Peclet number.

Accordingly, the dimensionless form of the Darcy-scale mode equations becomes:

$$(u_D,v_D)=\left[-\kappa_D\frac{\partial p_D}{\partial x_D},-\kappa_D\frac{\partial p_D}{\partial y_D}\right] \tag{20}$$

$$\frac{\partial\varphi}{\partial t_D}+\nabla.\mathbf{u}_D=0 \tag{21}$$

$$\frac{\partial(\varphi c_{fD})}{\partial t_D}+\nabla.(\mathbf{u}_D c_{fD})=-\frac{DaA_{vD}c_{fD}}{1+\frac{\phi^2 r_D}{Sh}}+\nabla.(\varphi\mathbf{D}_{eD}.\nabla c_{fD}) \tag{22}$$

$$\frac{\partial\varphi}{\partial t_D}=\frac{Da\,N_{ac}A_{vD}}{1+\frac{\phi^2 r_D}{Sh}}c_{fD} \tag{23}$$

$$D_{eD,X}=\frac{\alpha_{os}Da}{\Phi^2}+\frac{\lambda_x|\mathbf{u}_D|r_D\eta}{\varphi},\quad D_{eD,T}=\frac{\alpha_{os}Da}{\Phi^2}+\frac{\lambda_T|\mathbf{u}_D|r_D\eta}{\varphi} \tag{24}$$

$$Sh=Sh_\infty+0.7Re_p^{1/2}Sc^{1/3} \tag{25}$$

$$Re_p=\frac{\eta Pe}{Sc}|\mathbf{u}_D|r_D \tag{26}$$

$$\boldsymbol{\kappa}_D=\kappa_D\mathbf{I};\quad \kappa_D=\left(\frac{\varphi}{\varphi_0}\right)^{\gamma}\left[\frac{\varphi(1-\varphi_0)}{\varphi_0(1-\varphi)}\right]^{2\beta} \tag{27}$$

$$r_D=\sqrt{\frac{\kappa_D\varphi_0}{\varphi}} \tag{28}$$

$$A_{vD}=\frac{\varphi}{\varphi_0 r_D} \tag{29}$$

Moreover, the dimensionless boundary and initial conditions are:

$$c_{fD}-\varphi D_{eD,X}\frac{\partial c_{fD}}{\partial x_D}=1,\qquad \text{at } x_D=0 \tag{30}$$

$$-\kappa_D\frac{\partial p_D}{\partial x_D}=1,\quad \frac{\partial p_D}{\partial y_D}=0,\quad \text{at } x_D=0 \tag{31}$$

$$n.\nabla p_D=0,\quad n.\nabla c_{fD}=0,\quad \text{at } y_D=0,H/L \tag{32}$$

$$p_D=0,\quad \frac{\partial c_{fD}}{\partial x_D}=0,\qquad \text{at } x_D=1 \tag{33}$$

$$\varphi=\varphi_0+\hat{f},\quad c_{fD}=0,\qquad \text{at } t_D=0 \text{ and } \hat{f}\in[-\Delta\varphi_0,\Delta\varphi_0] \tag{34}$$

2.3. Fully implicit scheme

The fully implicit numerical scheme requires the system of nonlinear equations to be solved simultaneously. Accordingly, the 2D discretization of the Darcy-scale equations in the cartesian coordinates results in,

$$\left(u_{Di+1/2,j}^{t_D+\Delta t_D},v_{Di,j+1/2}^{t_D+\Delta t_D}\right)=\left[-\kappa_{Di+1/2,j}^{t_D+\Delta t_D}\frac{p_{Di+1,j}^{t_D+\Delta t_D}-p_{Di,j}^{t_D+\Delta t_D}}{x_{Di+1,j}-x_{Di,j}},-\kappa_{Di,j+1/2}^{t_D+\Delta t_D}\frac{p_{Di,j+1}^{t_D+\Delta t_D}-p_{Di,j}^{t_D+\Delta t_D}}{y_{Di,j+1}-y_{Di,j}}\right] \tag{35}$$

$$\frac{\varphi_{i,j}^{t_D+\Delta t_D}-\varphi_{i,j}^{t_D}}{\Delta t_D}+\frac{u_{Di+1/2,j}^{t_D+\Delta t_D}-u_{Di-1/2,j}^{t_D+\Delta t_D}}{x_{Di+1/2,j}-x_{Di-1/2,j}}+\frac{v_{Di,j+1/2}^{t_D+\Delta t_D}-v_{Di,j-1/2}^{t_D+\Delta t_D}}{y_{Di,j+1/2}-y_{Di,j-1/2}}=0 \tag{36}$$

$$\begin{aligned}&\frac{\varphi_{i,j}^{t_D+\Delta t_D}c_{fDi,j}^{t_D+\Delta t_D}-\varphi_{i,j}^{t_D}c_{fDi,j}^{t_D}}{\Delta t_D}+\frac{u_{Di+1/2,j}^{t_D+\Delta t_D}c_{fDi+1/2,j}^{t_D+\Delta t_D}-u_{Di-1/2,j}^{t_D+\Delta t_D}c_{fDi-1/2,j}^{t_D+\Delta t_D}}{x_{Di+1/2,j}-x_{Di-1/2,j}}+\\&\frac{v_{Di,j+1/2}^{t_D+\Delta t_D}c_{fDi,j+1/2}^{t_D+\Delta t_D}-v_{Di,j-1/2}^{t_D+\Delta t_D}c_{fDi,j-1/2}^{t_D+\Delta t_D}}{y_{Di,j+1/2}-y_{Di,j-1/2}}=\\&\frac{\varphi_{i+1/2,j}^{t_D+\Delta t_D}\mathbf{D}_{eDi+1/2,j}^{t_D+\Delta t_D}\nabla c_{fDi+1/2,j}^{t_D+\Delta t_D}-\varphi_{i-1/2,j}^{t_D+\Delta t_D}\mathbf{D}_{eDi-1/2,j}^{t_D+\Delta t_D}\nabla c_{fDi-1/2,j}^{t_D+\Delta t_D}}{x_{Di+1/2,j}-x_{Di-1/2,j}}\\&+\frac{\varphi_{i,j+1/2}^{t_D+\Delta t_D}\mathbf{D}_{eDi,j+1/2}^{t_D+\Delta t_D}\nabla c_{fDi,j+1/2}^{t_D+\Delta t_D}-\varphi_{i,j-1/2}^{t_D+\Delta t_D}\mathbf{D}_{eDi,j-1/2}^{t_D+\Delta t_D}\nabla c_{fDi,j-1/2}^{t_D+\Delta t_D}}{y_{Di,j+1/2}-y_{Di,j-1/2}}\\&-\frac{Da\,A_{vDi,j}^{t_D+\Delta t_D}}{1+\frac{\phi^2 r_{Di,j}^{t_D+\Delta t_D}}{Sh_{i,j}^{t_D+\Delta t_D}}}c_{fDi,j}^{t_D+\Delta t_D}\end{aligned} \tag{37}$$

$$\begin{aligned}\nabla c_{fDi+1/2,j}^{t_D+\Delta t_D}&=\frac{c_{fDi+1,j}^{t_D+\Delta t_D}-c_{fDi,j}^{t_D+\Delta t_D}}{x_{Di+1,j}-x_{Di,j}}\\\nabla c_{fDi-1/2,j}^{t_D+\Delta t_D}&=\frac{c_{fDi,j}^{t_D+\Delta t_D}-c_{fDi-1,j}^{t_D+\Delta t_D}}{x_{Di,j}-x_{Di-1,j}}\\\nabla c_{fDi,j+1/2}^{t_D+\Delta t_D}&=\frac{c_{fDi,j+1}^{t_D+\Delta t_D}-c_{fDi,j}^{t_D+\Delta t_D}}{y_{Di,j+1}-y_{Di,j}}\\\nabla c_{fDi,j-1/2}^{t_D+\Delta t_D}&=\frac{c_{fDi,j}^{t_D+\Delta t_D}-c_{fDi,j-1}^{t_D+\Delta t_D}}{y_{Di,j}-y_{Di,j-1}}\end{aligned} \tag{38}$$

$$\frac{\varphi_{i,j}^{t_D+\Delta t_D}-\varphi_{i,j}^{t_D}}{\Delta t_D}=\frac{Da\,N_{ac}A_{vDi,j}^{t_D+\Delta t_D}}{1+\frac{\phi^2 r_{Di,j}^{t_D+\Delta t_D}}{Sh_{i,j}^{t_D+\Delta t_D}}}c_{fDi,j}^{t_D+\Delta t_D} \tag{39}$$

in which $i=1,2\ldots,N_x$ and $j=1,2\ldots,N_y$; N_x and N_y are the number of gridblocks in the x and y directions, respectively. All the variables are assumed to be at time step $t_D+\Delta t_D$. Also, a 2D staggered grid is considered (Fig. 1) wherein pressures are defined at the grid centers while the velocities are defined at the grid boundaries.

In the staggered grid technique, the scalar variables (porosity, pressure, and concentration) are defined at the grid centers, while the velocities are stored at the grid faces. On the contrary, all variables are located at the same points in the collocated grid techniques. The staggered grid technique is mainly used to avoid odd-even decoupling between the scalar and the vector variables. Odd-even decoupling, also known as checkerboard pattern, odd–even grid oscillation, grid-scale oscillation, and zig-zag form, is a kind of discretization error that frequently happens in the collocated grid techniques [25]. Accordingly, the acquired solution alternatively fluctuates along the gridblocks. This fluctuation deteriorates the accuracy and instability of the numerical solution [26].

In reactive flow through porous media, the acid reacts with the rock matrix and dissolves the rock minerals as it is transported through the domain. Accordingly, structural properties of the porous medium change continuously, and wormholes are propagated throughout the carbonate rock. Therefore, the acid transport and its reaction are inherently coupled here. Also, the fully implicit scheme requires the system of nonlinear equations to be solved simultaneously. Thus, a number of five coupled partial differential equations should be discretized and solved simultaneously to compute the evolution of porosity [17, 20]. Consequently, the fully implicit scheme is highly complicated and challenging. Moreover, an extremely fine mesh structure is required to well capture the acid front. For example, Sahu et al. [28] considered 42,000 mesh grids for a 2D rock sample of size 5 cm × 2 cm. Actually, an order of Φ^2 number of grids is at least required in the direction of acid injection. Accordingly, for a large rock sample or fast reactive fronts, a large number of gridblocks are required which poses a high computational burden.

2.4. Method of lines

The basic idea in this study is to solve the system of coupled

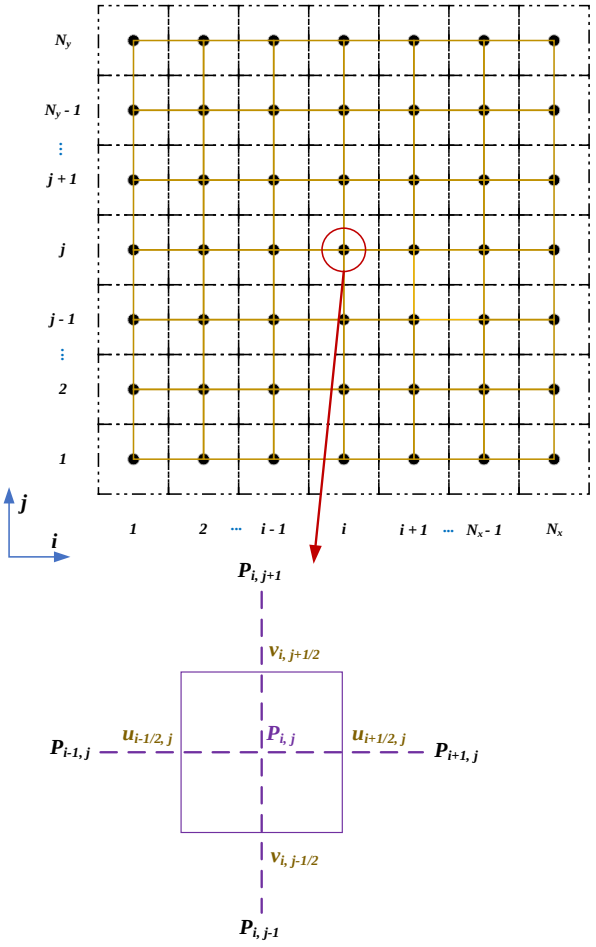

Fig. 1. The schematic of 2D staggered grid.

differential equations using the MOL. In the MOL, only the spatial variables of the governing partial differential equations are discretized and the time variable remains continuous. Consequently, the partial differential equations are transformed into ordinary ones which are then numerically solved by high-order Runge-Kutta methods. Compared to the fully implicit scheme, the MOL is less complicated and more straightforward. Also, the computational cost is more affordable.

Accordingly, the 1D discretization of the Darcy-scale equations simplifies to (time index of the variables are removed for simplicity):

$$\frac{Da\,N_{ac}A_{vDi}}{1+\frac{\phi^2 r_{Di}}{Sh_i}}c_{fDi}+\frac{u_{Di+1/2}-u_{Di-1/2}}{x_{Di+1/2}-x_{Di-1/2}}=0 \tag{40}$$

$$\varphi_i\frac{\partial c_{fDi}}{\partial t_D}=-\frac{u_{Di+1/2}c_{fDi+1/2}-u_{Di-1/2}c_{fDi-1/2}}{x_{Di+1/2}-x_{Di-1/2}}+\frac{\varphi_{i+1/2}\mathbf{D}_{eDi+1/2}\nabla c_{fDi+1/2}-\varphi_{i-1/2}\mathbf{D}_{eDi-1/2}\nabla c_{fDi-1/2}}{x_{Di+1/2}-x_{Di-1/2}}-\frac{Da\,A_{vD}}{1+\frac{\phi^2 r_{Di}}{Sh_i}}\left(c_{fDi}+N_{ac}c_{fDi}^2\right) \tag{41}$$

$$\nabla c_{fDi+1/2}=\frac{c_{fDi+1}-c_{fDi}}{x_{Di+1}-x_{Di}}$$
$$\nabla c_{fDi-1/2}=\frac{c_{fDi}-c_{fDi-1}}{x_{Di}-x_{Di-1}} \tag{42}$$

$$\frac{\partial\varphi_i}{\partial t_D}=\frac{Da\,N_{ac}A_{vDi}}{1+\frac{\phi^2 r_{Di}}{Sh_i}}c_{fDi} \tag{43}$$

There are three variables (u_D, φ, c_{fD}) with three equations. Therefore, pressure variable is removed and fluid velocity is directly computed from the continuity equation. Consequently, Eqs. 41 and 43 are simultaneously used to calculate both acid concentration and porosity evolution.

Similarly, the 2D discretization of the Darcy-scale equations by the MOL approach becomes:

$$\left(u_{Di+1/2,j},v_{Di,j+1/2}\right)=\left[-\kappa_{Di+1/2,j}\frac{p_{Di+1,j}-p_{Di,j}}{x_{Di+1,j}-x_{Di,j}},-\kappa_{Di,j+1/2}\frac{p_{Di,j+1}-p_{Di,j}}{y_{Di,j+1}-y_{Di,j}}\right] \tag{44}$$

$$\frac{Da\,N_{ac}A_{vDi,j}}{1+\frac{\phi^2 r_{Di,j}}{Sh_{i,j}}}c_{fDi,j}+\frac{u_{Di+1/2,j}-u_{Di-1/2,j}}{x_{Di+1/2,j}-x_{Di-1/2,j}}+\frac{v_{Di,j+1/2}-v_{Di,j-1/2}}{y_{Di,j+1/2}-y_{Di,j-1/2}}=0 \tag{45}$$

$$\varphi_{i,j}\frac{\partial c_{fDi,j}}{\partial t_D}=-\frac{u_{Di+1/2,j}c_{fDi+1/2,j}-u_{Di-1/2,j}c_{fDi-1/2,j}}{x_{Di+1/2,j}-x_{Di-1/2,j}}-\frac{v_{Di,j+1/2}c_{fDi,j+1/2}-v_{Di,j-1/2}c_{fDi,j-1/2}}{y_{Di,j+1/2}-y_{Di,j-1/2}}+\frac{\varphi_{i+1/2,j}\mathbf{D}_{eDi+1/2,j}\nabla c_{fDi+1/2,j}-\varphi_{i-1/2,j}\mathbf{D}_{eDi-1/2,j}\nabla c_{fDi-1/2,j}}{x_{Di+1/2,j}-x_{Di-1/2,j}}+\frac{\varphi_{i,j+1/2}\mathbf{D}_{eDi,j+1/2}\nabla c_{fDi,j+1/2}-\varphi_{i,j-1/2}\mathbf{D}_{eDi,j-1/2}\nabla c_{fDi,j-1/2}}{y_{Di,j+1/2}-y_{Di,j-1/2}}-\frac{Da\,A_{vD}}{1+\frac{\phi^2 r_{Di,j}}{Sh_{i,j}}}\left(c_{fDi,j}+N_{ac}c_{fDi,j}^2\right) \tag{46}$$

$$\nabla c_{fDi+1/2,j}=\frac{c_{fDi+1,j}-c_{fDi,j}}{x_{Di+1,j}-x_{Di,j}}$$
$$\nabla c_{fDi-1/2,j}=\frac{c_{fDi,j}-c_{fDi-1,j}}{x_{Di,j}-x_{Di-1,j}}$$
$$\nabla c_{fDi,j+1/2}=\frac{c_{fDi,j+1}-c_{fDi,j}}{y_{Di,j+1}-y_{Di,j}}$$
$$\nabla c_{fDi,j-1/2}=\frac{c_{fDi,j}-c_{fDi,j-1}}{y_{Di,j}-y_{Di,j-1}} \tag{47}$$

$$\frac{\partial\varphi_{i,j}}{\partial t_D}=\frac{Da\,N_{ac}A_{vDi,j}}{1+\frac{\phi^2 r_{Di,j}}{Sh_{i,j}}}c_{fDi,j} \tag{48}$$

Here, there are five variables $(p_D, u_D, v_D, \varphi, c_{fD})$ with five equations. Initially, p_D, u_D and v_D are calculated from Eqs. Afterwards, Eqs. 46 and 47 are simultaneously used to only calculate the acid concentration and porosity evolution.

2.4.1. Runge-Kutta method

Runge–Kutta (RK) methods are efficient, long-established, and popular techniques for numerical analyzing initial-value problems in differential equations [21]. The RK technique establishes high order precise solutions by the function itself, and requires none of the function derivatives. In this study, the sixth-order RK method is used to compute the acid concentration and porosity evolution in the 1D and 2D models [27],

$$\text{if } \Theta'=\Psi(t,\Theta)$$
$$\text{then: } \Theta^{n+1}=\Theta^n+\frac{\Delta t}{90}\left(7k_1+32k_3+12k_4+32k_5+7k_6\right) \tag{49}$$

where,

$$
\begin{aligned}
k_1 &= \Psi\left(t^n, \Theta^n\right) \\
k_2 &= \Psi\left(t^n + \frac{\Delta t}{2}, \Theta^n + \frac{\Delta t}{2} k_1\right) \\
k_3 &= \Psi\left(t^n + \frac{\Delta t}{4}, \Theta^n + \frac{\Delta t}{16}\left(3k_1 + k_2\right)\right) \\
k_4 &= \Psi\left(t^n + \frac{\Delta t}{2}, \Theta^n + \frac{\Delta t}{2} k_3\right) \\
k_5 &= \Psi\left(t^n + \frac{3\Delta t}{4}, \Theta^n + \frac{\Delta t}{16}\left(-3k_2 + 6k_3 + 9k_4\right)\right) \\
k_6 &= \Psi\left(t^n + \Delta t, \Theta^n + \frac{\Delta t}{7}\left(k_1 + 43k_2 + 6k_3 - 12k_4 + 8k_5\right)\right)
\end{aligned} \tag{50}
$$

2.5. Analytical solution

An analytical solution of the dissolution front is also possible if, 1) the rock sample is 1D, 2) the dispersion coefficient (De) and mass transfer coefficient (kc) are assumed to be independent of the flow velocity, and 3) initial porosity is assumed to be homogeneous throughout the domain. The derivation of the 1D analytical solution is thoroughly described by Maheshwari et al. [11]. Actually, analytical solution is considered to verify the proposed approach in this study.

3. Model Description

3.1. Case 1: 1D core model

First, the MOL approach proposed in this study is compared against the analytical solution by Maheshwari et al. [11]. The associated parameters are listed in Table 1. Also, the initial porosity of the domain is homogeneous.

3.2. Case 2: 2D core model

After the verification of the MOL approach, it will be utilized to investigate the effect of multiple transport and reaction phenomena on the matrix acidizing in carbonate formations. The initial porosity field is uniformly distributed with an average value of 0.2. Again, the associated parameters are listed in Table 1.

Table 1. 1D and 2D model parameters.

Variable	Unit	1D model	2D model
a_0	[1/cm]	50	50
b	[-]	0.7	0.7
C_0	[mol/L]	4.2	4.2
D_m	[cm²/s]	3.6×10^{-5}	3.6×10^{-5}
H	[in]	-	1.5
k_0	[mD]	10	5
k_s	[cm/s]	1.4×10^{-4}	1.4×10^{-4}
L	[in]	5	4
r_o	[μm]	5	5
Sh_∞	[-]	3	3
u_0	[cm/s]	2×10^{-4}	1×10^{-3}
α_{os}	[-]	0.5	0.5
α	[g/mol]	50	50
β	[-]	1	2
γ	[-]	1	1
λ_x	[-]	0.5	0.5
λ_y	[-]	0.1	0.1
μ	[cP]	1	1
ρ_s	[g/cm³]	2.71	2.71
ν	[cm²/s]	0.01	0.01
ρ	[g/cm³]	1	1
φ_0	[-]	0.2	0.2
$\Delta\varphi_0$	[-]	0	0.08

4. Results and Discussions

4.1. Case 1: 1D core model

Fig. 2 compares between the MOL results and the analytical solution after 28 pore volumes of the acid injection. The injected pore volume is calculated from:

$$\text{PVINJ} = \frac{Q_{inj} \times t}{PV} \tag{51}$$

where Q_{inj} shows the injected acid flowrate and PV shows the pore volume of rock sample.

The blue line illustrates the results from the analytical solution, while the red squares represent the dissolution front from the MOL. The plots on the left are porosity versus x_D, and those on the right show c_{fD} versus x_D for different values of Da. A piston-like displacement is observed, and there is a close agreement between the MOL results and the analytical solution which verifies the successful implementation of the MOL method. Also, the dissolution front becomes sharper as the value of Da increases.

4.2. Case 2: 2D core model

A uniform porosity field with an average of 0.2 is distributed throughout the domain. A coarse grid cannot adequately capture the acid front and wormhole propagation. Grid size testing is then utilized to determine the minimum number of required gridblocks. Therefore, the accuracy of the numerical solution was examined at different grid sizes by comparing the pore volumes of the injected acid. Accordingly, a number of 250 × 85 grids is considered for the 2D core model.

Fig. 3 represents the porosity maps at different times for hydrochloric acid 15%. Expectedly, the entrance face of rock first reacts with the injected acid, initiating tiny channels. Afterwards, the acid reacts with the calcite minerals and expands the channels. Specifically, one of the channels grows rapidly and becomes the dominant flow for the injected acid. Accordingly, the injected acid goes mainly through that principal channel due to its lower resistance to flow. The width and the size of the channels are increased as more acid is injected through the rock sample. The simulation process is terminated whenever the breakthrough of acid is observed at the right face of the rock. Similarly, acid concentration maps at different times are depicted in Fig. 4.

The breakthrough time is considered the time at which overall permeability is increased by a factor of 100, or overall pressure drop is decreased by the same factor [11, 28]. Thereafter, the injected pore volume to breakthrough (PVTB) is computed from Eq.51.

In carbonate matrix acidizing, the PVTB is an important indicator of assessing acidizing performance. Expectedly, an ideal acidizing scenario contains the minimum volume of injected acid with maximum wormholes lengths. Fig. 5 illustrates the overall permeability and pressure drop along the core versus time. First, the overall permeability of the core gradually increases, indicating the dissolution of rock minerals by the injected acid. Afterwards, the exponential promotion in rock permeability reveals the breakthrough of acid at the outlet face. Here, a conductive channel is created across the core, connecting the inlet face to the outlet one. At the same time, the pressure drop across the core significantly decreases, as further depicted in Fig. 6.

The injection rate of acid affects the dissolution pattern and morphology of the wormholes, as illustrated in Fig. 7 and Fig. 8. Actually, the rate of acid injection affects the Damkohler and Peclet numbers. The Damkohler number shows the ratio of convective to reaction times. Accordingly, low values of Da indicates high rates of acid injection and low reactivity. Specifically, at Da = 1, the transport and reaction phenomena are balanced and the rock porosity increases but no channel is created. Actually, the residence time of acid is less than the required reaction time, resulting in incomplete dissolution of carbonate rock minerals. Therefore, the injected acid reaches almost all the points of the rock sample, resulting in a uniform increase in the rock porosity. This pattern is called a uniform dissolution pattern, meaning that acid convection dominates the dispersion. On the contrary, high values of Da

indicates low rates of acid injection and high reactivity. At *Da* = 500, complete dissolution of rock minerals is achieved due to the large soaking time of the acid. In other words, reactive solution is mostly used up in a thin region around the acid front. This is referred to as the face dissolution pattern, meaning that the dispersion of acid dominates its convection, and a single conical wormhole is observed. Accordingly, the amount of acid required to make a conductive path across the core approaches that of the completely dissolving the rock sample. However, at intermediate injection rates, there is a competition between dispersion, convection, and reaction. Accordingly, acid wormholes are created meaning that only some parts of the rock minerals are dissolved by the acid which results in fewer volumes of required acid to increase the rock permeability.

Compared to the fully implicit scheme, such as the study of Sahu et al. [28], the MOL is less complicated and more straightforward. Also, the computational cost is more affordable. According to Sahu et al. [28], simulation times for a 2D rock sample of size 5 cm × 2 cm on a workstation ranged between 0.5 to 24 hours. In the current study, however, all the simulation times were below one hour on a desktop computer.

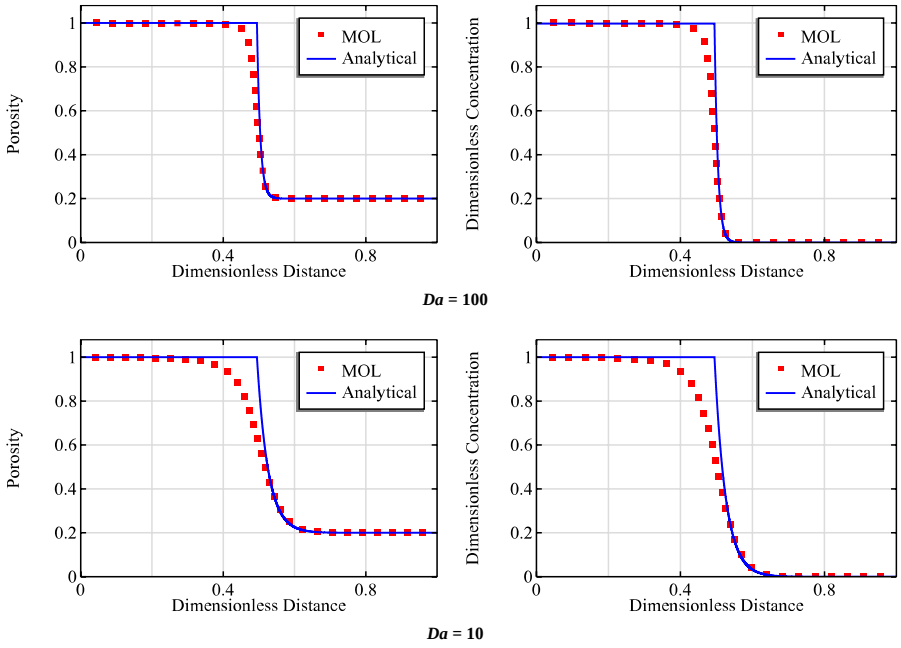

Fig. 2. Comparison between the MOL and analytical solutions after 28 pore volumes of the acid injection.

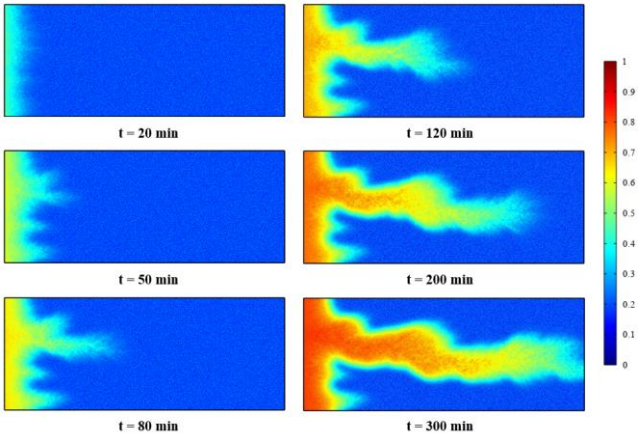

Fig. 3. The porosity maps at different times.

5. Conclusions

In this study, the MOL approach was utilized to characterize the dissolution of rock minerals and wormhole propagation in carbonate rocks using the Darcy scale model. Accordingly, only the spatial variables of the governing partial differential equations were discretized and the time variable remained continuous. Consequently, the partial differential equations become ordinary ones and were then numerically solved by the sixth-order RK method.

The MOL approach was first verified against the analytical solution in a 1D core model. Thereafter, it was utilized to investigate the effect of multiple transport and reaction phenomena on the matrix acidizing in carbonate formations. Furthermore, the staggered grid technique was employed to accurately predict wormhole patterns during different injection regimes. Compared to the fully implicit scheme, the MOL is less complicated and more straightforward. Also, the computational burden is inexpensive. According to Sahu et al. [28], simulation times for a 2D rock sample of size 5 cm × 2 cm on a workstation ranged between 0.5 to 24 hours. In the current work, however, all the simulation times for a 2D rock sample of size 4 in × 1.5 in were below one hour on a desktop computer.

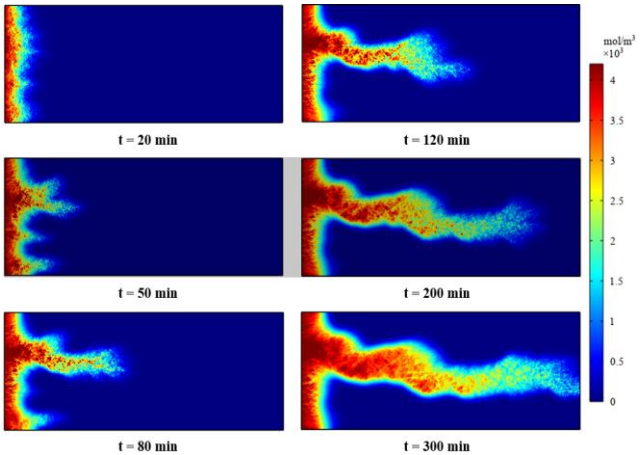

Fig. 4. The acid concentration maps at different times.

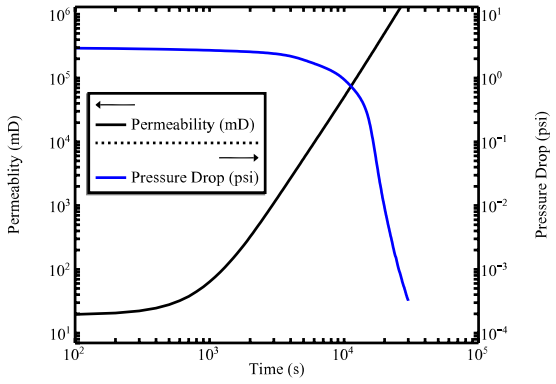

Fig. 5. Overall permeability and pressure drop along the core versus time.

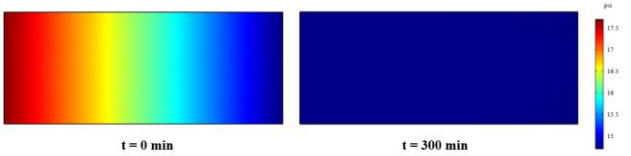

Fig. 6. The pressure maps at two different times.

Furthermore, upscaling of the MOL approach to the wellbore scale, and considering thermal effects and multi-layer reservoirs are regarded as the future directions for the current study. In addition, multiphase version of the Darcy's law should be implemented to consider the impact of CO_2 evolution.

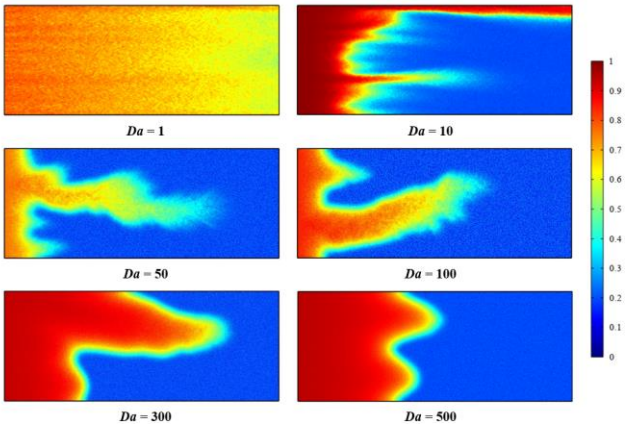

Fig. 7. The effect of *Da* on morphology of the wormholes and porosity maps.

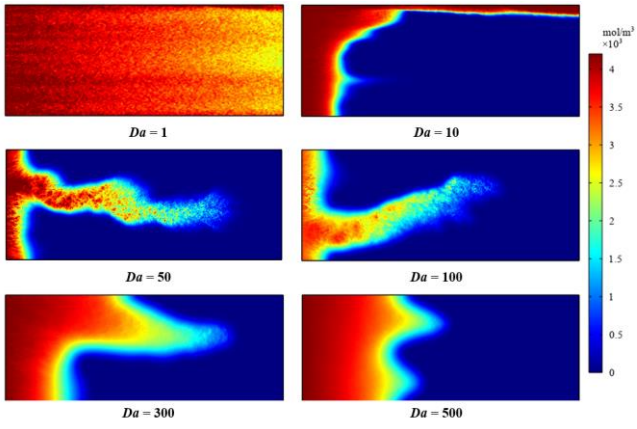

Fig. 8. The effect of *Da* on morphology of the wormholes and concentration maps.

REFERENCES

[1] Ahmed T., Reservoir engineering handbook, 5th ed., Gulf Professional Publishing, Boston, 2018. https://doi.org/10.1016/C2016-0-04718-6.

[2] Ganat T.A.A.O., Modern Pressure Transient Analysis of Petroleum Reservoirs Springer, 2023. https://doi.org/10.1007/978-3-031-28889-0.

[3] Schön J.H., Physical properties of rocks: Fundamentals and principles of petrophysics, Elsevier, 2015. https://doi.org/10.1029/97EO00363.

[4] Jia C., Sepehrnoori K., Huang Z., Zhang H., Yao J., Numerical studies and analysis on reactive flow in carbonate matrix acidizing, J Petrol Sci Eng, 201 (2021) 108487. https://doi.org/10.1016/j.petrol.2021.108487.

[5] Barri A., Hassan A., Mahmoud M., Carbonate Stimulation Using Chelating Agents: Improving the Treatment Performance by Optimizing the Fluid Properties, ACS omega, 7 (2022) 8938-8949. https://doi.org/10.1021/acsomega.1c07329.

[6] Tariq Z., Aljawad M.S., Hassan A., Mahmoud M., Al-Ramadhan A., Chelating agents as acid-fracturing fluids: experimental and modeling studies, Energy Fuels, 35 (2021) 2602-2618. https://doi.org/10.1021/acs.energyfuels.0c04045.

[7] Yoo H., Kim Y., Lee W., Lee J., An experimental study on acid-rock reaction kinetics using dolomite in carbonate acidizing, J Petrol Sci Eng, 168 (2018) 478-494. https://doi.org/10.1016/j.petrol.2018.05.041.

[8] Qiu X., Aidagulov G., Ghommem M., Edelman E., Brady D., Abbad M., Towards a better understanding of wormhole propagation in carbonate rocks: Linear vs. radial acid injection, J Petrol Sci Eng, 171 (2018) 570-583. https://doi.org/10.1016/j.petrol.2018.07.075.

[9] Wu Y., Salama A., Sun S., Parallel simulation of wormhole propagation with the Darcy–Brinkman–Forchheimer framework, Comput Geotech, 69 (2015) 564-577. https://doi.org/10.1016/j.compgeo.2015.06.021.

[10] Liu P., Yao J., Couples G.D., Ma J., Iliev O., 3-D modelling and experimental comparison of reactive flow in carbonates under radial flow conditions, Sci Rep, 7 (2017) 17711. https://doi.org/10.1038/s41598-017-18095-2.

[11] Maheshwari P., Ratnakar R., Kalia N., Balakotaiah V., 3-D simulation and analysis of reactive dissolution and wormhole formation in carbonate rocks, Chem Eng Sci, 90 (2013) 258-274. https://doi.org/10.1016/j.ces.2012.12.032.

[12] Daccord G., Lenormand R., Lietard O., Chemical dissolution of a porous medium by a reactive fluid—I. Model for the "wormholing" phenomenon, Chem Eng Sci, 48 (1993) 169-178. https://doi.org/10.1016/0009-2509(93)80293-Y.

[13] Hung K., Hill A., Sepehrnoori K., A mechanistic model of wormhole growth in carbonate matrix acidizing and acid fracturing, J Pet Technol, 41 (1989) 59-66. https://doi.org/10.2118/16886-PA.

[14] Tansey J., Balhoff M.T., Pore network modeling of reactive transport and dissolution in porous media, Transp Porous Media, 113 (2016) 303-327. https://doi.org/10.1007/s11242-016-0695-x.

[15] Algive L., Bekri S., Vizika O., Pore-network modeling dedicated to the determination of the petrophysical-property changes in the presence of reactive fluid, SPE J, 15 (2010) 618-633. https://doi.org/10.2118/124305-PA.

[16] Panga M.K., Ziauddin M., Balakotaiah V., Two - scale continuum model for simulation of wormholes in carbonate acidization, AlChE J, 51 (2005) 3231-3248. https://doi.org/10.1002/aic.10574.

[17] Jia C., Huang Z., Sepehrnoori K., Yao J., Modification of two-scale continuum model and numerical studies for carbonate matrix acidizing, J Petrol Sci Eng, 197 (2021) 107972. https://doi.org/10.1016/j.petrol.2020.107972.

[18] Fredd C.N., Fogler H.S., Influence of transport and reaction on wormhole formation in porous media, AIChE J, 44 (1998) 1933-1949. https://doi.org/10.1002/aic.690440902.

[19] Hoefner M., Fogler H.S., Pore evolution and channel formation during flow and reaction in porous media, AlChE J, 34 (1988) 45-54. https://doi.org/10.1002/aic.690340107.

[20] Kalia N., Balakotaiah V., Effect of medium heterogeneities on reactive dissolution of carbonates, Chem Eng Sci, 64 (2009) 376-390. https://doi.org/10.1016/j.ces.2008.10.026.

[21] Chapra S.C., Canale R.P., Numerical methods for engineers, McGraw-Hill, New York, 2021.

[22] Mahmoodi A., Javadi A., Sola B.S., Porous media acidizing simulation: New two-phase two-scale continuum modeling approach, J Petrol Sci Eng, 166 (2018) 679-692. https://doi.org/10.1016/j.petrol.2018.03.072.

[23] Safari M., Gholami R., Jami M., Ananthan M.A., Rahimi A., Khur W.S., Developing a porosity-permeability relationship for ellipsoidal grains: A correction shape factor for Kozeny-Carman's equation, J Petrol Sci Eng, 205 (2021) 108896. https://doi.org/10.1016/j.petrol.2021.108896.

[24] Balakotaiah V., West D.H., Shape normalization and analysis of the mass transfer controlled regime in catalytic monoliths, Chem Eng Sci, 57 (2002) 1269-1286. https://doi.org/10.1016/S0009-2509(02)00059-3.

[25] Reiss J., A Family of Energy Stable, Skew-Symmetric Finite Difference Schemes on Collocated Grids: A Simple Way to Avoid Odd–Even Decoupling, J Sci Comput, 65 (2015) 821-838. https://doi.org/10.1007/s10915-015-9985-7.

[26] Tang H., Dong W., Agrawal A., A phenomenon of artificial odd–even grid oscillation and its presence in domain decomposition computation: Algebraic analysis and numerical illustration, J Comput Appl Math, 333 (2018) 404-427. https://doi.org/10.1016/j.cam.2017.10.017.

[27] Adegboye Z., Yahaya Y., Ahmed U., Direct integration of general fourth order ordinary differential equations using fifth order runge-kutta method, J Niger Math Soc, 39 (2020) 69-78.

[28] Sahu Q., Fahs M., Hoteit H., Optimization and uncertainty quantification method for reservoir stimulation through carbonate acidizing, ACS Omega, 8 (2022) 539-554. https://doi.org/10.1021/acsomega.2c05564.